Supplementary Information for: Structure-Performance Relationships of Lithium-Ion Battery Cathodes Revealed by Contrast-Variation Small-Angle Neutron Scattering

Qingsong Liu [†a], Willa Brenneis [†a], Gergely Nagy [b], Mathieu Doucet [b],

Jeffrey Lopez*[a], Jeffrey J. Richards*[a]

[†]: Q.L. and W.B. contributed equally to this work

[a]. Department of Chemical and Biological Engineering, Northwestern University, Evanston, IL, 60208

[b]. Neutron Scattering Division, Oak Ridge National Laboratory, Oak Ridge, TN, 37831

*. Authors to whom correspondence should be addressed; electronic mails:

jlopez@northwestern.edu

jeffrey.richards@northwestern.edu

SI.1. Structural Characterization of Carbon Black (CB)

The transmission electron microscopy (TEM) image of CB Super C65 is shown in Fig. S1A. An example primary particle is highlighted, and the histogram of the primary particle size is presented in the inset, from which we calculated the average primary particle diameter D_p as 35.6 ± 8.2 nm. We show the small-angle neutron scattering (SANS) measurement of 3 wt% CB in N-methyl-2-pyrrolidone (NMP) in Fig. S1B. To identify the interface regions, we plot Porod's plot in Fig. S1C which shows two plateau regions, suggesting that interfaces at two length scales exist. The first interface, in the length scale of 31 to 52 nm, can be assigned to the solvent/CB interface, and the second interface, in the length scale of 9 to 14 nm, can be attributed to the internal pores of CB. In Fig S1D, we present the Kratky plot of the same SANS profile in Fig S1B. We notice that the transition from the primary aggregate to the agglomerate appears at the Q value of 0.004 $Å^{-2}$, corresponding to a real-space distance of 157 nm. As discussed in the main text, this transition to probing the CB agglomerate structure is quantitatively consistent with the length scale at which the addition of solvent changes the CB structure.

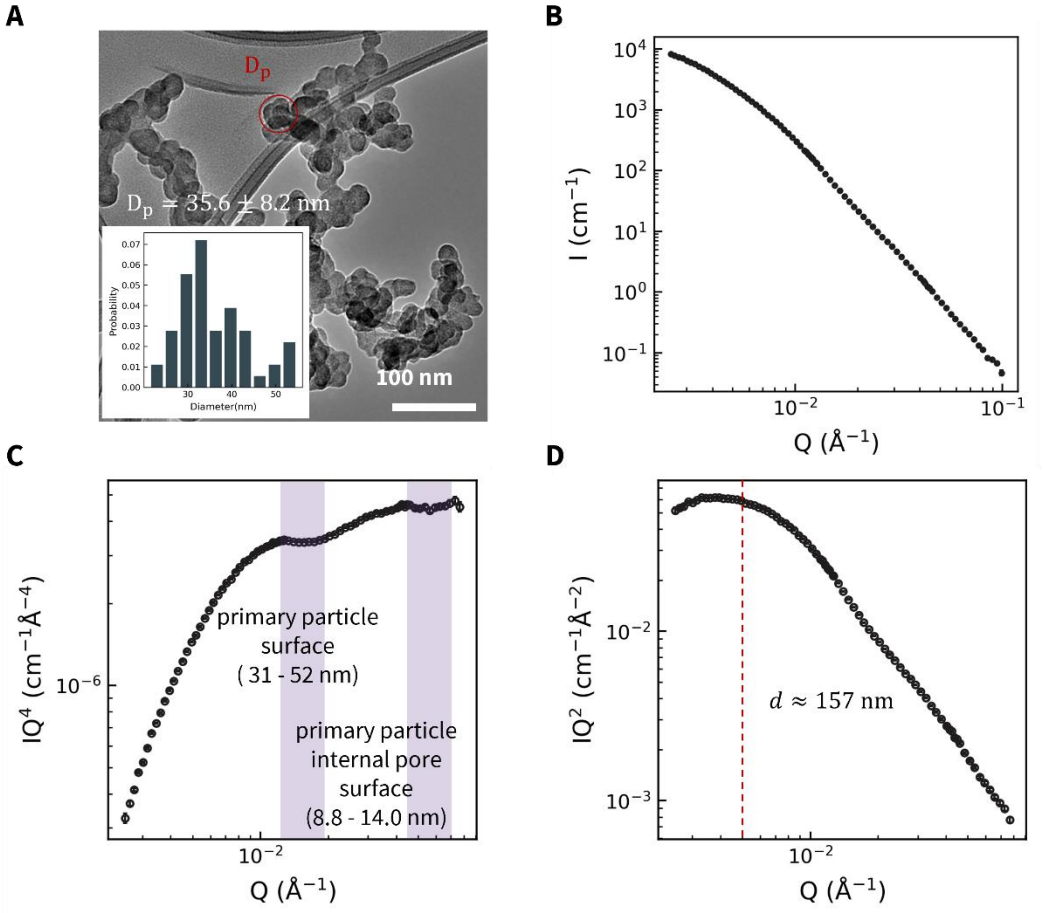

Figure S1. **Structural characterization of CB.** (A) TEM of CB. An example primary particle is highlighted. Inset: Size distribution of CB primary particles. (B) Background and incoherent scattering subtracted SANS curve of 3 wt% CB in NMP (C) Porod's plot of 3 wt% CB in NMP. Two plateaus indicate Porod's scattering at two length scales. (D) Kratky plot of 3 wt% CB in NMP. The transition length scale from probing CB primary aggregate to agglomerate internal structure is indicated with a red dotted line. This transition length scale is calculated to be about 157 nm.

SI.2. Structural Characterization of Active Material (AM)

Scanning electron microscopy (SEM) image of AM NMC811 ($LiNi_{0.8}Mn_{0.1}Co_{0.1}O_2$) is shown in Fig. S2A. The histogram of the AM particle size is shown in Fig. S2B, and we calculate an average diameter of 6.8 ± 2.8 µm. In Fig. S2C, we show the Porod's plots of 3 wt% CB in NMP added with different amounts of $LiNi_{0.8}Mn_{0.8}Co_{0.8}O_2$ (NMC811) characterized by ultra small-angle X-ray scattering (USAXS, Argonne 9ID)[1], as it is impossible to measure only NMC811 suspended in NMP due to strong sedimentation. We notice that the addition of NMC811 only significantly modifies the scattering intensity at larger length scales (< 0.001 Å^{-2}) while in the hypothesized region of measuring solid/solvent interface (highlighted in shade), Porod's plots remain to have consistent plateaus in the shaded region, suggesting that the mixture of CB/AM interface can still be well described by Porod's law.

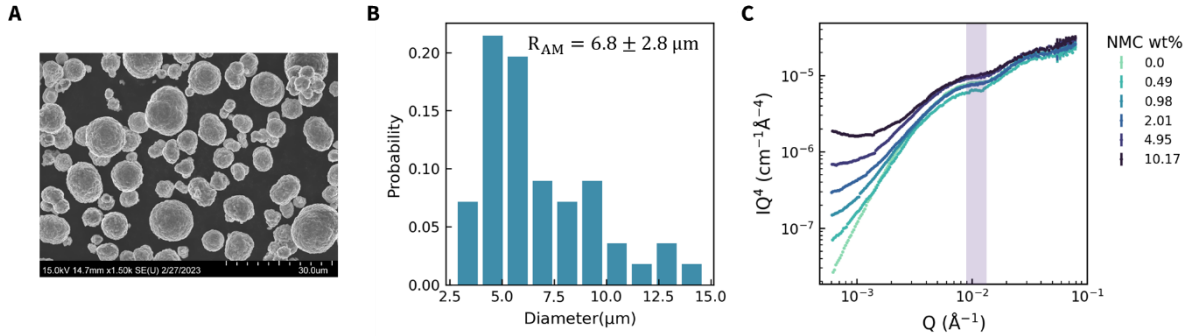

Figure S2. Structural characterization of NMC 811. (A) SEM of NMC 811 particles. (B) Size distribution of NMC811. (C) Porod's plots of USAXS measurements of CB/NMC811 suspensions in NMP at different NMC811 loadings. The power-law slope in the interface length scale remains constant.

SI.3. Data Analysis with the Generalized Porod's Scattering Law Method (GPSLM)

In GPSLM[2], the constant $C_P(\rho_f) = IQ^4$ is obtained from each scattering curve in the Porod's region. The intensity ratio is then given as

$$IR = C_P(\rho_s)/C_P(\rho_s = 0) \qquad (S1)$$

which is fit to a quadratic function of solvent scattering length density ρ_s,

$$IR(\rho_s) = \frac{1}{{\rho_{2M}}^2}(\rho_s - \rho_A)^2 + \Delta H^2 \qquad (S2).$$

ρ_A represents the surface-area averaged scattering length density of the solvent-accessible surface, defined as

$$\rho_A \equiv \frac{\int \rho(S) dS}{S} \quad (S3),$$

where S is the interface, and ${\rho_{2M}}^2$ is the surface-area averaged squared scattering length density, defined as

$${\rho_{2M}}^2 \equiv \frac{\int \rho(S)^2 dS}{S} \qquad (S4).$$

ΔH^2, calculated as

$$\frac{{\rho_{2M}}^2 - {\rho_A}^2}{{\rho_{2M}}^2} \qquad (S5),$$

represents the degree of heterogeneity. This method has been shown to characterize materials with smooth interface[3] and coarse interface[4]. In the coarse interface case, only the ρ_A and a modified solvent-accessible surface area can be obtained. The exact relationship between the modified surface area (which depends on the exact length scale and the surface fractal dimension) and the true surface area has not been determined. Furthermore, when other structural scattering contributions are convoluted, GPSLM[2] proposes to subtract the solvent-independent inhomogeneity by using the differences between the measurements at different solvent scattering length densities and the measurement at 0 ρ_s.

SI.4. Derivation of generalized contrast-variation method

For a sample composed of a solid phase and a liquid phase, the measured scattering intensity can be written as

$$I(Q) = \iint g(\mathbf{r}_i)\, g(\mathbf{r}_j)\, \frac{\sin(Q\mathbf{r}_{ij})}{Q\mathbf{r}_{ij}}\, d\mathbf{r}_i\, d\mathbf{r}_j \quad \text{(S6)},$$

where $g(\mathbf{r})$ is the excess density that describes the contribution of the solid phase when the inhomogeneity in the solvent phase is much smaller than the length scale probed in small-angle neutron scattering (SANS). The equation above reflects the information obtained from SANS measurements: the sum of any two-point correlation weighted by the scattering length density (ρ_m) within the measured sample. $g(\mathbf{r})$ is determined by both the solvent penetration (ϕ_m) and the solvent scattering length density (ρ_s) in the form of

$$g(\mathbf{r}) = \phi_m(\mathbf{r})(\rho_m(\mathbf{r}) - \rho_s(\mathbf{r})) \qquad \text{(S7)}.$$

When expanded as a function of ρ_s, $I(Q)$ can be rewritten as

$$I(Q, \rho_s) = {\rho_s}^2 I_1(Q) - 2\rho_s I_{01}(Q) + I_0(Q) \quad \text{(S8)}.$$

The form of the above expansion was first proposed by Stuhrman[5] and extensively discussed by Feigin and Svergun[6] for particles suspended in a solvent. The definition of each basic function is given as:

$$I_1 = \iint \phi_m(\mathbf{r}_i)\, \phi_m(\mathbf{r}_j)\, \frac{\sin(Q\mathbf{r}_{ij})}{Q\mathbf{r}_{ij}}\, d\mathbf{r}_i\, d\mathbf{r}_j \qquad \text{(S9)}$$

$$I_{01} = \iint \phi_m(\mathbf{r}_i)\, \phi_m(\mathbf{r}_j)\rho_m(\mathbf{r}_i)\, \frac{\sin(Q\mathbf{r}_{ij})}{Q\mathbf{r}_{ij}}\, d\mathbf{r}_i\, d\mathbf{r}_j \qquad \text{(S10)}$$

$$I_0 = \iint \phi_m(\mathbf{r}_i)\, \phi_m(\mathbf{r}_j)\rho_m(\mathbf{r}_i)\rho_m(\mathbf{r}_j)\, \frac{\sin(Q\mathbf{r}_{ij})}{Q\mathbf{r}_{ij}}\, d\mathbf{r}_i\, d\mathbf{r}_j \quad (11).$$

We applied this analysis to all measured electrodes. The chemical and structural parameters obtained are presented in Table S1.

Table S1: Solvent-accessible surface area (S_T) and the surface-averaged scattering length density (ρ_A) at this interface

		Slurry Solids Content	Surface-averaged scattering length density (ρ_A, 10^{-6} Å^{-2})	Error	Surface Area (S_T, m^2/g)	Error
Calendered	High Shear	38	5.756	0.239	1.588	0.012
		42	5.161	0.126	2.245	0.010
		46	5.997	0.241	1.438	0.011
	Low Shear	38	6.125	0.240	1.463	0.011
		42	5.745	0.155	1.843	0.009
		46	5.862	0.168	1.878	0.010
Uncalendered	High Shear	38	6.226	0.315	1.182	0.011
		42	5.184	0.145	2.011	0.010
		46	5.956	0.252	1.426	0.011
	Low Shear	38	6.300	0.257	1.420	0.011
		42	5.748	0.170	1.723	0.010
		46	5.875	0.192	1.655	0.010

SI.5. The Relationships Between the Generalized Contrast-Variation Method and Other Existing Contrast-Variation Methods

Two main methods that utilize contrast-variation SANS are the Generalized Porod's Scattering Law method (GPSLM)[2–4] and the Stuhrmann method[7], which are used to characterize the porous interface and the particle radius of gyration respectively. Here in this note, we will show the correlation between the generalized contrast-variation method and the two methods.

In the GPSLM method, a smooth surface's scattering can be written as

$$I = C_P Q^{-4} \qquad \text{(S12)},$$

where C_P is defined as

$$C_P = 2\pi\langle\Delta\rho\rangle^2 S_T \qquad \text{(S13)}.$$

S_T is the specific surface area, and $\Delta\rho$ is the scattering length density difference between the surface (ρ) and the solvent (ρ_S). The generalized contrast-variation method can be written as

$$I(Q,\rho_s) = {\rho_s}^2 2\pi S_T - 2\rho_s 2\pi\langle\rho\rangle S_T + 2\pi\langle\rho^2\rangle S_T \qquad \text{(S14)}.$$

The intensity ratio defined in the GPSLM method can be expressed as

$$\frac{I(Q,\rho_S)}{I(Q,\rho_S=0)} = \frac{{\rho_s}^2 - 2\rho_s*\langle\rho\rangle + \langle\rho^2\rangle}{\langle\rho^2\rangle} \qquad \text{(S15)},$$

which can then be rearranged into

$$\frac{I(Q,\rho_S)}{I(Q,\rho_S=0)} = \frac{1}{\langle\rho^2\rangle}(\rho_s - \langle\rho\rangle)^2 + \frac{\langle\rho^2\rangle - \langle\rho\rangle^2}{\langle\rho^2\rangle} \qquad \text{(S16)}.$$

This form is the same as the GPSLM and shows that the generalized contrast-variation method is equivalent to the GPSLM in the surface scattering region.

Deriving the Stuhrmann method from the generalized contrast-variation method requires the modification of the excess function $g(\mathbf{r})$, which now has a form of

$$g(\mathbf{r}) = \Delta\rho\phi_m(\mathbf{r}) + \rho_f(\mathbf{r}) \qquad \text{(S17)}.$$

$\phi_m(\mathbf{r})$ for a particle is given as

$$\phi_m(\mathbf{r}) = \begin{cases} 1, & \mathbf{r} \text{ within particle} \\ 0, & \mathbf{r} \text{ outisde particle} \end{cases} \qquad \text{(S18)}.$$

$\rho_f(\mathbf{r})$ is the excess scattering length density, defined as $\rho_m(\mathbf{r}) - \overline{\rho_m(\mathbf{r})}$. Expanding the scattering into a similar form as the generalized contrast-variation method yields

$$I(Q) = \Delta\rho^2 I_c(Q) + \Delta\rho I_{cs}(Q) + I_s(Q) \qquad \text{(S19)},$$

which can then be written as

$$R_g = R_c + \frac{\alpha}{\Delta\rho} - \frac{\beta}{\Delta\rho^2} \qquad \text{(S20)}$$

in the Guinier region[6], where α and β describe the inhomogeneity within the particles.

SI.6 Mercury Intrusion Porosimetry & Porosity

SANS measurements indicate that calendering, which applies shear deformation to the CBD microstructure, reduces the CB fractal agglomerate dimension to open the CB nanoscale structure (Fig. 3C). We corroborate these findings with mercury intrusion porosimetry (MIP) plotted in Fig. S3, where we see an increase in the differential intrusion volume of 50 – 100 nm-diameter pores after Calendering, corresponding to an expansion of CB structure despite an overall reduction in porosity.

MIP was conducted by MSE Analytical Services using a MicroActive AutoPore V 9600 and a 0254 - (13) 3 Bulb Penetrometer. Sample masses ranged from 0.1381 to 0.2671 g. Measurements were collected from 0.10 to 61,000.00 psi at 25 °C. The porosities shown in Fig. S3 and Table S2 were calculated using a measured density of each cathode sample compared to the theoretical bulk density.

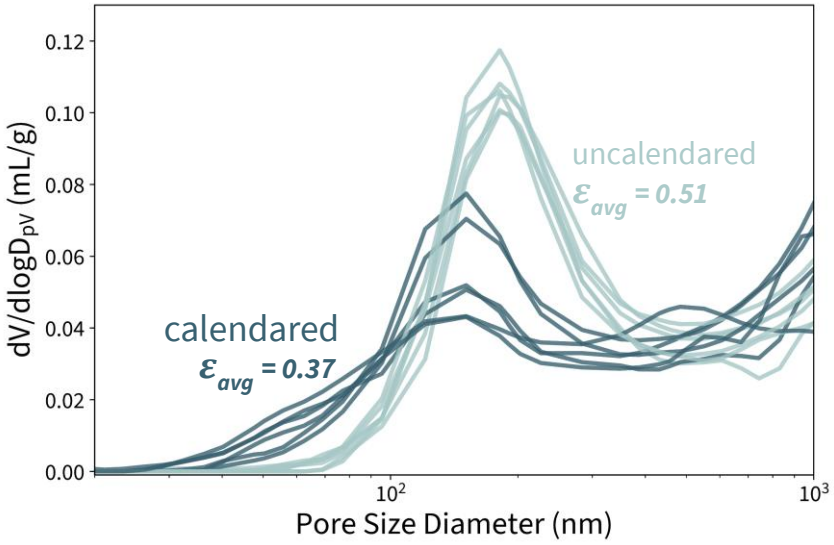

Figure S3. Differential Intrusion volume across pore diameter from mercury intrusion porosimetry. Intrusion volume for pores with diameters in the range of 50 - 100 nm increases after calendaring.

Table S2: Porosity of each cathode sample. Calculated by comparing theoretical bulk density and true density of each cathode.

		Slurry Solids Content (%)	Porosity (ε)			Slurry Solids Content (%)	Porosity (ε)
Calendered	High Shear	38	0.398	Uncalendered	High Shear	38	0.605
		42	0.252			42	0.658
		46	0.315			46	0.558
	Low Shear	38	0.407		Low Shear	38	0.611
		42	0.407			42	0.582
		46	0.427			46	0.566

SI.7. Structural Parameters of Electrodes from SANS Measurements

To extract useful structural parameters from measured SANS parameters, we construct a simple model that can calculate the amount of each species present at the solvent interface. In this model, the varying scattering length density and specific surface area present in each electrode are attributed to two main contributions: dense agglomeration of CB which leads to surface area loss (1-θ of the surface area lost), and binder covering the surface of CB (χ for how much of CB surface is covered by the binder, and ξ for the thickness of the binder layer). In addition, size distribution information of AM and CB obtained from TEM and SEM above is utilized in the model as known parameters to calculate surface area per unit weight. Without any agglomeration or structuring, the 'pristine' surface area of AM and CB per unit weight electrode is $S_{AM,p}$ (0.137*0.90 m^2/g) and $S_{CB,p}$ (82.91*0.05 m^2/g). We further assume that 10% of the AM particles are covered by the carbon/binder domain. While this assumption is necessary to determine binder PVDF and CB surface areas and fractions, the exact value of this assumption does not impact our conclusions (SI.8).

Therefore, the area lost due to carbon/binder domain contact is $S_{contact} = S_{AM,p} * 0.1$. In this model, three equations are needed to solve the three parameters θ, χ, and ξ. The first equation of the model constraints that the total surface area per unit weight (S_T) present at the interface equal to the specific surface area from SANS. Due to the non-agglomerating nature of AM, AM's surface contribution is simply $S_{AM,p} - S_{contact}$. Accounting for the agglomeration of CB and the coverage of the binder, CB's surface contribution can be written as $\theta(1-\chi)S_{CB,p} - S_{contact}/2$, where the surface area lost due to domain contact is assumed to be equally split between the uncovered CB and CB covered by binder. Lastly, for the CB covered by the binder, the specific surface area will scale down with increasing binder thickness as $S_{CB,p}\frac{R_p}{R_p+\xi}$. Together, the first equation is written as:

$$\left(S_{AM,p} - S_{contact}\right) + \left(\theta(1-\chi)S_{CB,p} - S_{contact}/2\right) + \left(\theta\chi S_{CB,p}\frac{R_p}{R_p+\xi} - S_{contact}/2\right) = S_T \quad \text{(S10).}$$

The second equation utilizes the average scattering length density (SLD_A) obtained from the SANS measurements at the interface. The sum of each species' contribution equals the multiplication of SLD_A and S_T. Therefore, the second equation can be written as:

$$\left(S_{AM,p} - S_{contact}\right)SLD_{AM} + \left(\theta(1-\chi)S_{CB,p} - S_{contact}/2\right)SLD_{CB} + \left(\theta\chi S_{CB,p}\frac{R_p}{R_p+\xi} - S_{contact}/2\right)SLD_B = S_T SLD_A \quad \text{(S11).}$$

We further set a third equation to conserve the mass balance of the binder present in a unit mass of the electrode. The total volume of binder covering the CB surface equals the volume of binder per CB particle $\frac{4\pi}{3}\left(\left(R_p+\xi\right)^3 - {R_p}^3\right)$ multiplied by the number of CB particles covered ($N_{CB}\theta\chi$), where N_{CB} is calculated as $\frac{S_{CB,p}}{4\pi {R_p}^2}$. Therefore, the third equation can be written as:

$$\frac{4\pi}{3}\left(\left(R_p+\xi\right)^3 - {R_p}^3\right)N_{CB}\theta\chi = \rho_B * w_B \quad \text{(S12),}$$

where ρ_B is the binder density (1.76 g/cm^3), and w_B the weight fraction of PVDF (5%). To calculate the surface area presented at the interface for each species, we can use the following equations:

$$S_{CB} = \theta(1-\chi)S_{CB,p} - S_{contact}/2 \quad \text{(S13)}$$

$$S_B = \theta\chi S_{CB,p}\frac{R_p}{R_p+\xi} - S_{contact}/2 \quad \text{(S14).}$$

The calculated parameters for each electrode are presented in Table 1 in the manuscript. The broad variation in scattering-based structural characteristics across cathode coating conditions confirms the fabrication of varying cathode microstructures. For example, Calendering in most cases increases the total surface area and reduces PVDF layer thickness but has a less obvious impact on CB and PVDF surface areas. Low shear coating rates increase the solvent-accessible CB surface area while high shear increases PVDF surface area in most cases. Calendering decreases PVDF layer thickness in electrodes with low slurry solids content, but the effect is less pronounced with higher solids content. The presence of distinct microstructures evidenced by SANS-based structural parameters promises further application of this tool to optimize cathode processing conditions to reach desired structural characteristics.

SI.8. Validation of Conclusions with Varying AM Surface Coverage Assumptions and Cycle Numbers

To solve for PVDF and CB surface contributions distinctly, we were required to assume the degree of AM surface that was inaccessible to solvent. In the final model, we assumed that 10% of the AM surface was inaccessible based on literature[8]. To validate our conclusions regardless of the exact value of this assumption, we examine the CB SA under three assumptions of surface coverage: 0%, 10%, or 20%. As shown in Fig. S4, the trend in CB SA across coating conditions and electrochemical performance remains the same regardless of the exact value assumed, validating our conclusions based on Fig. 4 in the main text.

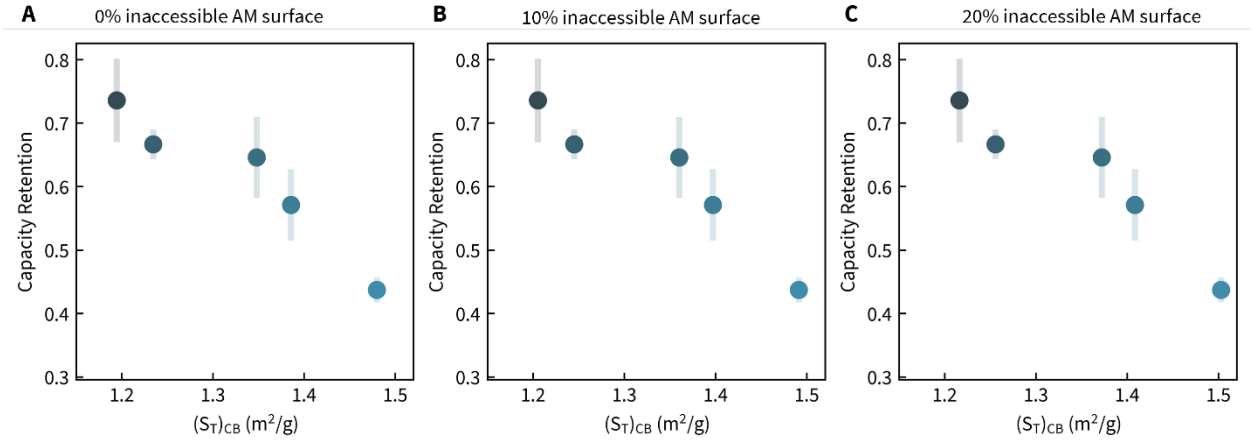

Figure S4. A) Specific carbon black surface area assuming 0% of AM surface is inaccessible to solvent B) assuming 10% of AM surface is inaccessible to solvent C) assuming 20% of AM surface is inaccessible to solvent.

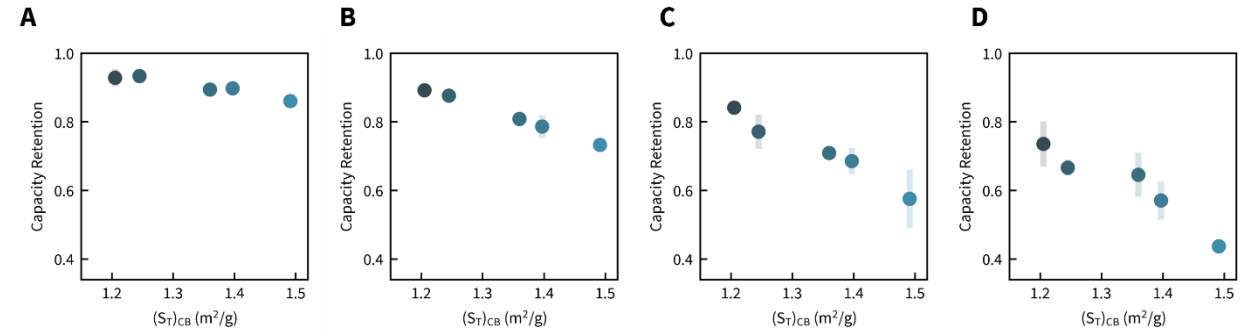

Figure S5. Specific carbon black surface area and capacity retention after A) 40 cycles, B) 60 cycles, C) 80 cycles, and D) 100 cycles.

Further, to confirm that the degradation of capacity after many cycles could be correlated to the extent of exposed carbon black surface area, we examine this relationship across the lifetime of the cathodes. Fig. S5 presents the capacity retention after increasing cycle numbers compared to the exposed specific carbon black surface area, and the correlation presented in the main text is consistent across the cell lifetime, lending confidence to our derived correlation.

SI.9. Capacitance Obtained from Blocking Electrolyte Impedance Spectroscopy

To validate scattering structural parameters, we examined the electrochemical impedance spectroscopy (EIS) of cathodes at each coating condition. EIS was performed in triplicate for each cathode coating condition. CR2032 coin cells (MTI corp.) were prepared in a glovebox (O_2 < 0.5 ppm, H_2O < 0.05 ppm) and were constructed as symmetric cells with two, identical, 12 mm composite cathode discs, a glass fiber separator (VWR), and 200 µl of electrolyte (10 mmol tetrabutylammonium hexafluorophosphate ($TBAPF_6$, Sigma) in ethylene carbonate (EC, gotion) and dimethyl carbonate (DMC, gotion) (1:1 w:w)). $TBAPF_6$ was selected as a non-intercalating electrolyte salt to ensure blocking conditions. Each cell was left to rest for 12 hours in an environmental chamber (Espec) set to 25ºC. EIS was measured at 25ºC and open circuit voltage (OCV) from 1 MHz to 100 MHz with a 10 mV perturbation.

An example EIS plot is shown in Fig. S6A & B. We then construct an equivalent circuit (Fig. S6C) which entails a resistor, a resistor/capacitor (RC) unit, and an ionic diffusion part described by a transmission line model. The transmission line model at low frequencies follows the analysis of porous electrodes by Ogihara et al.[11] and Landesfiend et al.[12]. The overall equivalent circuit can then be written as:

$$Z = R_0 + \frac{R_1}{1+(i\omega\tau)^{n_1}} + \sqrt{\frac{R_{ion}}{Q_s(i\omega)^{n_2}}}\coth\left(\sqrt{Q_s(i\omega)^{n_2}R_{ion}}\right) \qquad \text{(S15)},$$

where R is the resistance, τ the relaxation time, n is the exponent, and Q_s is the capacitance.

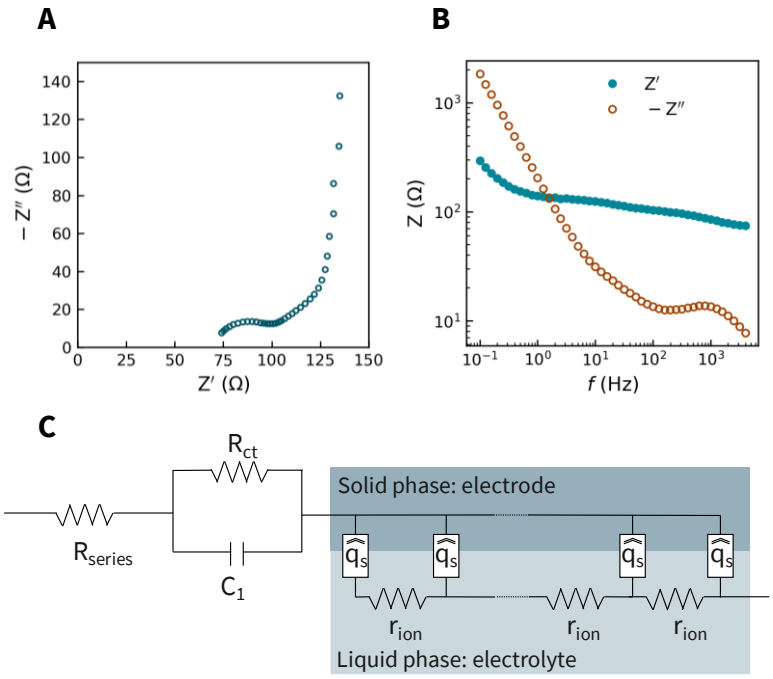

Figure S6. A) Nyquist plot for a single example of impedance response for the cathode in a symmetric cell B) Bode plot demonstrating real and imaginary impedance spectra. C) Illustration of the equivalent circuit transmission-line model used to fit impedance response.

The impedance spectroscopy data were fitted with a population-based Markov chain Monte Carlo method which utilizes Differential Evolution Adaptive Metropolis scheme (DREAM)[13]

within the frequency range of 0.1 to 5000 Hz. This fitting algorithm shows high ergodicity[13] and fitted error estimations can be obtained. In Fig. S7A & B, we show the fitted results superimposed on the original data. We also show the correlation plots of all parameters fitted in Fig S7C. Except for the parameters which are mathematically correlated in the equations, such as R_1 and n_1, all other parameters show weak correlations, as indicated by the isotropic correlation plots. Fig S7C further supports the robustness of the fitting algorithm.

For each condition, we extract the surface constant-phase capacitance, Q_s. We find that surface capacitance is strongly correlated to scattering-based solvent-accessible CB surface area (Fig. S8). As CB is much more electronically conductive than AM, we expect the majority of surface charging to be attributed to solvent-accessible CB surface area[14]. We find a good agreement with the literature for CB capacitance (0.023 F/m^2 in our case (Fig. S8), 0.021 F/m^2 reported by Oswald et al.[14] using impedance methods), assuming fully capacitive behavior. This correlation demonstrates good agreement between EIS and scattering-based structural measurements and validates our quantitative analysis of cathode structural parameters.

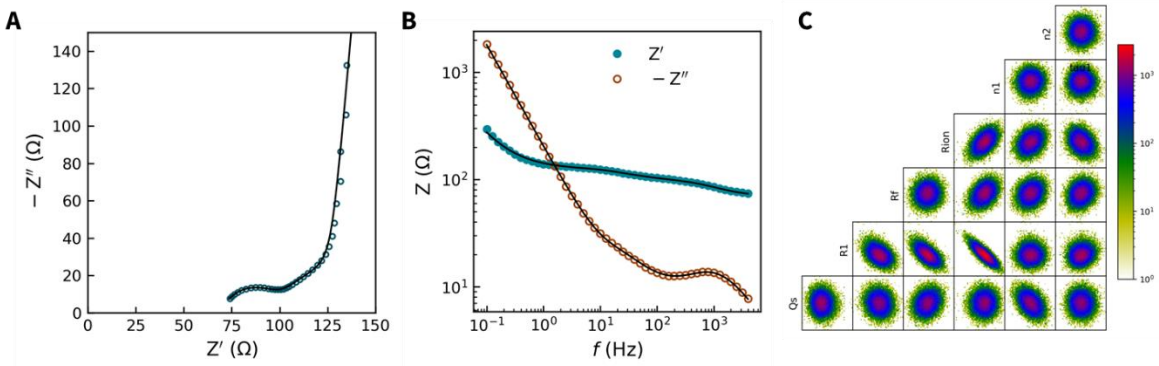

Figure S7. A) example of transmission-line model (solid line) fitted to experimental EIS data (open circles). B) Fit model and EIS data separated by real and imaginary impedance. C) Correlation plots of all fitted parameters generated by the DREAM fitting algorithm.

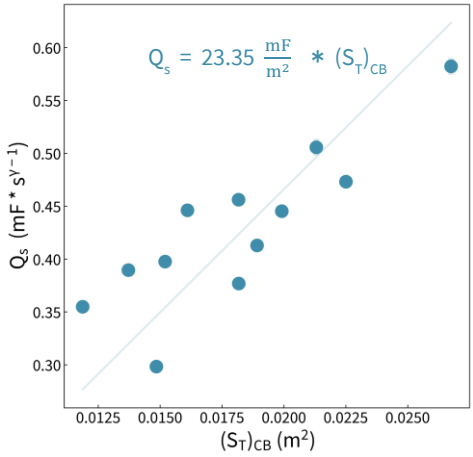

Figure S8. SANS-based carbon-black surface area demonstrates good agreement with both EIS-based surface capacitance and literature-based carbon-black capacitance[14].

SI.10. Electrode Coating Parameters & Loading

Composite cathodes were fabricated with varying slurry solids content, coating shear rate, and degree of Calendering. The slurry solids content was controlled using various PVDF in NMP solution concentrations, and and refers to the percentage of solid material (NMC, CB, PVDF) in the NMP slurry. Solids content varied from 38% to 46%. The shear rate was controlled by blade coater speed. Cathodes coated at maximum blade speed are denoted as "High Shear," coated at a shear rate of 874.9 1/s. Cathodes coated at minimum blade speed are denoted as "Low Shear," coated at a shear rate of 13.1 1/s. Calendered electrodes were processed with a single pass through a roll press with a gap height of 0.1 mm. All electrodes were punched into 12 mm discs (area = 1.13 cm^2) to be constructed into coin cells.

Table S3: Coating Parameters and Loading of Composite Cathodes

		Slurry Solids Content (%)	Mass Loading (mg/cm^2)	Areal Capacity (mAh/cm^2)	Thickness (μm)
Calendered	High Shear	38	10.06	1.91	36.6
		42	11.82	2.25	34.4
		46	12.07	2.29	38.6
	Low Shear	38	12.90	2.45	47.6
		42	14.24	2.71	52.6
		46	15.86	3.01	60.6
Uncalendered	High Shear	38	10.06	1.84	56.6
		42	10.73	2.04	68.6
		46	11.64	2.21	57.6
	Low Shear	38	13.08	2.48	73.6
		42	13.49	2.56	70.6
		46	14.40	2.74	72.6

References

1. Ilavsky, J. *et al.* Development of combined microstructure and structure characterization facility for in situ and operando studies at the advanced photon source. *J Appl Crystallogr* **51**, 867–882 (2018).

2. Chiang, W. S., Chen, J. H. & Liu, Y. Investigation of porous materials with large surface heterogeneity using the generalized porod's scattering law method. *Phys Rev E* **99**, (2019).

3. Chiang, W. S., Georgi, D., Yildirim, T., Chen, J. H. & Liu, Y. A non-invasive method to directly quantify surface heterogeneity of porous materials. *Nat Commun* **9**, (2018).

4. Chiang, W. S. *et al.* Structural Properties of Kerogens with Different Maturities. *Energy and Fuels* **34**, 12354–12365 (2020).

5. Stuhrmannz, H. B. & Kirste, R. G. Elimination der intrapartikulären Untergrundstreuung bei der Röntgenkleinwinkelstreuung an kompakten Teilchen. II. *Zeitschrift fur Physikalische Chemie* **56**, 334–337 (1967).

6. Feigin, L. A. & Svergun, D. I. *Structure Analysis by Small-Angle X-Ray and Neutron Scattering*. (Springer US, 2013).

7. Stuhrmann, H. B. & IUCr. Neutron small-angle scattering of biological macromolecules in solution. *urn:issn:0021-8898* **7**, 173–178 (1974).

8. Komini Babu, S., Mohamed, A. I., Whitacre, J. F. & Litster, S. Multiple imaging mode X-ray computed tomography for distinguishing active and inactive phases in lithium-ion battery cathodes. *J Power Sources* **283**, (2015).

9. Lu, X. *et al.* Effect of carbon blacks on electrical conduction and conductive binder domain of next-generation lithium-ion batteries. *J Power Sources* **592**, 233916 (2024).

10. Sim, R., Lee, S., Li, W. & Manthiram, A. Influence of Calendering on the Electrochemical Performance of LiNi0.9Mn0.05Al0.05O2Cathodes in Lithium-Ion Cells. *ACS Appl Mater Interfaces* **13**, (2021).

11. Ogihara, N. *et al.* Theoretical and Experimental Analysis of Porous Electrodes for Lithium-Ion Batteries by Electrochemical Impedance Spectroscopy Using a Symmetric Cell. *J Electrochem Soc* **159**, A1034–A1039 (2012).

12. Landesfeind, J., Hattendorff, J., Ehrl, A., Wall, W. A. & Gasteiger, H. A. Tortuosity Determination of Battery Electrodes and Separators by Impedance Spectroscopy. *J Electrochem Soc* **163**, A1373–A1387 (2016).

13. Vrugt, J. A. *et al. Accelerating Markov Chain Monte Carlo Simulation by Differential Evolution with Self-Adaptive Randomized Subspace Sampling*. *International Journal of Nonlinear Sciences & Numerical Simulation* vol. 10 (2009).

14. Oswald, S. *et al.* Novel Method for Monitoring the Electrochemical Capacitance by In Situ Impedance Spectroscopy as Indicator for Particle Cracking of Nickel-Rich NCMs: Part I. Theory and Validation. *J Electrochem Soc* **167**, 100511 (2020).